Data-Driven Modeling of Sub-Cycle Dynamics of Inverter-based Resources Using Real-World Synchro-Waveform Measurements

Hossein Mohsenzadeh-Yazdi, *Student Member, IEEE*, Fatemeh Ahmadi-Gorjayi, *Student Member, IEEE*, and Hamed Mohsenian-Rad, *Fellow, IEEE*

***Abstract*—As inverter-based resources (IBRs) become increasingly integrated into modern power systems, there is a growing need for adept modeling techniques that can accurately capture their dynamic response to disturbances. In this paper, three novel *data-driven* methods are proposed to model the dynamic response of IBRs during *sub-cycle* disturbances. We use real-world voltage and current waveform data from waveform measurement units (WMUs) installed at IBRs at a test site in California. The proposed methods are designed based on long short-term memory (LSTM) networks. They vary in terms of the architecture of the LSTM networks and the feature extraction characteristics. Furthermore, two methods are proposed to reuse or adjust a model from one IBR to capture the response of another IBR based on the analysis of *time-synchronized* waveform measurements at two IBRs. The results demonstrate that despite the model being constructed based on a different IBR, the proposed methods exhibit high accuracy. Experimental results demonstrate and validate the high accuracy of the models and provide a comparison with recent data-driven methods in the literature.**

***Keywords*: Inverter-based resources, data-driven modeling, dynamic response, sub-cycle oscillations, LSTM, clustering, WMU, waveform measurements, synchro-waveforms, real-world data.**

I. Introduction

With the advent of Waveform Measurement Units (WMUs), high-resolution, time-synchronized waveform measurements are becoming available in practice [1]. A WMU provides GPS time-stamped samples of voltage or current waveforms, with sampling rates from 64 to 512 samples per cycle [2], [3]. WMU measurements are highly valuable in monitoring the fast dynamic behavior of Inverter-Based Resources (IBRs) in response to *transient disturbances* in power systems. Such complex transient dynamics *cannot* be adequately captured by traditional Supervisory Control and Data Acquisition (SCADA) devices or Phasor Measurement Units (PMUs) [4].

In fact, the North American Electric Reliability Corporation (NERC) has recently reported several system-wide incidents due to the unexpected dynamic response of IBRs to transient disturbances [5]. Post-mortem analysis, as in [6] and [7], has revealed the need for high-resolution waveform data at IBRs, including during *short-lasting* and *sub-cycle* disturbances.

Therefore, there is a growing need to develop and validate IBR models that can provide high-fidelity predictions of IBR behavior during sub-cycle disturbances. Such models have various applications, including in power quality [8], [9], power system protection [10], [11], and power system stability [12].

The authors are with the Department of Electrical and Computer Engineering, University of California, Riverside, CA, USA. This work is supported in part by the CEC grant EPC-16-077 and NSF grant ECCS 2330155. The corresponding author is H. Mohsenian-Rad. E-mail: hamed@ece.ucr.edu.

In this paper, we utilize WMU measurements at a test site in California to model the dynamic response of IBRs to sub-cycle oscillatory disturbances. However, obtaining accurate models is challenging due to the complexity of IBR dynamics. In fact, the lack of reliable waveform-level models (even black-box models) for IBRs is a key obstacle to ensure proper network operation during faults and disturbances; see [13].

We address this shortcoming by taking a *data-driven* approach, relying solely on waveform measurements *without* access to the physical models of the internal components of the IBRs. We use *real-world* waveform measurements during sub-cycle oscillatory disturbances and the corresponding responses of commercial IBRs in California. In addition to building models to predict the dynamic behavior of the IBR, we also explore the technical options to reuse models across different IBRs. The latter capability is achieved by taking advantage of *time-synchronized* waveform measurements from multiple IBR locations during the *same* system-wide disturbance.

A. Literature Review

Physics-based models are traditionally used for modeling the dynamics of IBRs; e.g., see [14]–[16]. However, they require access to precise models of the internal components and the internal control loops of the IBR. They may also face practical challenges, such as computational complexity [17].

A recent alternative to physics-based modeling is *data-driven* methods. Some data-driven methods are hybrid, i.e., they use field data to identify the parameters of a physical model [18]. Hence, they may still require some prior knowledge about the IBR. Furthermore, hybrid model accuracy often depends on whether the measurements can accurately estimate the intended physical parameters, e.g., see [19].

There are recent data-driven models that do *not* require physics-based modeling. The method in [20] uses PMU (not WMU) data to model the dynamics of IBRs. Since the focus in [20] is on phasors (not waveforms), it cannot capture the dynamics of transient sub-cycle events. In [21], regression and modal analysis are used to capture IBR dynamics using WMU data. In [22], a Nonlinear AutoRegressive with eXogenous input Neural Network is used to predict the response of IBRs during various dynamic physical events. The analysis in [22] is based on data from PMUs (not WMUs). However, we still use a variation of the method in [22] as one of the baselines for performance comparison in this paper. We refer to it as the Nonlinear Neural Network Regression method to contrast it with the Multi-Model Linear Regression method in [21], which is another baseline for our performance comparison.

Another approach to data-driven modeling of IBRs is impedance models. Impedance models often assume a linear relationship between voltage and current. Hence, they often need to assume a specific operating point [23]. An alternative approach was recently proposed in [24], where the impedance model of an IBR is developed as a polynomial (hence nonlinear) function. However, impedance-based models are primarily used for analyzing harmonic stability and short-term stability related to IBRs, which is a different domain from the dynamic response modeling that is the focus in this paper.

In this paper, we use Long Short-Term Memory (LSTM) networks [26], where we devise new LSTM architectures to model the dynamics of IBRs. LSTM is a type of Recurrent Neural Network (RNN) that is specifically designed to handle sequential data and time series. LSTMs extend the short-term memory capability of RNNs by introducing a gating mechanism (forget, input, and output gates) to enhance performance and identify longer temporal connections between input and output. LSTMs are particularly effective at learning long-term dependencies and nonlinear patterns within time series data.

LSTM networks have been used in many applications in power systems, such as for transient stability assessment [27], enhanced situational awareness [28], load forecasting [29], partial discharge detection [30], solar generation forecasting [31], detecting High Impedance Faults [32], and modeling the dynamics of the RMS values of voltage and current in a voltage-regulated variable-load DC/DC buck converter [33]. However, to the best of our knowledge, LSTM has not been used to model sub-cycle IBR dynamics using synchrowaveform measurements. However, with proper architecture design and feature extraction, LSTM can be suitable in this area, as we will show in detail throughout this paper.

Last but not least, since this paper provides a novel data-driven application of WMU measurements, the relevant literature also includes the studies in the emerging field of WMU data analytics, such as for the purpose of event detection and characterization [34], [35], fault location identification [36]–[38], analysis of resonance [39], analysis of partial discharge [40], wildfire mitigation [41], and frequency estimation [42].

B. Summary of Contributions and Key Results

Three different approaches are proposed to model the sub-cycle dynamic behavior of IBRs. *Approach 1* extracts the nonlinear relationship between the time series of the sub-cycle differential voltage (input) and the time series of the sub-cycle differential current (output) at the IBR. *Approach 2* extends Approach 1 with a new architecture and new features to capture the *pre-disturbance state of operation* of the IBR. This is achieved by creating an *additional layer* in the LSTM architecture in Approach 1. *Approach 3* further extends Approach 2, by constructing *multiple models* to choose from, through clustering of the training events, and developing a method for *model selection* for any given test data.

We use *real-world waveform measurements* to evaluate the performance of the proposed methods. Approach 1 reduces the average modeling error by 37% compared to [21], and by 3% compared to [22], which are both based on *regression analysis*. This error can be further reduced by 68% in Approach 2; because Approach 2 can capture the pre-disturbance state of operation of the IBR. Approach 3 reduces the error by another 18% due to its model selection capabilities.

Using real-world measurements is necessary. Simulations are inherently limited to capturing only those dynamics that are already included in the simulated models. They cannot capture all physical phenomena in real-world systems, such as unknown, unmodeled, or highly complex interactions that exceed the simulation's assumptions and computational feasibility. In fact, using simulated data may defeat the purpose of this study. This study is motivated by a real-world challenge: grid operators struggle to predict the dynamic response of IBRs based on field measurements, especially in the absence of sophisticated physics-based models, which are often unavailable for most customer-owned IBRs. Using real-world data is crucial to addressing this real-world challenge.

In addition to building models that accurately predict the dynamic behavior of individual IBRs, we also explore technical approaches to enable model reuse across different IBRs. This capability is facilitated by leveraging the WMU's ability to provide *time-synchronized* waveform measurements from multiple IBR locations during the same system-wide disturbance. Such analysis is particularly important for capturing the dynamics of IBRs that serve as Grid Edge Resources (GERs), where utilities often have limited observability.

Compared to the conference version of this work in [43], this journal version has several new analyses and results. Approach 3, which has the best performance, is completely new. The core ideas are to cluster the training events, and accordingly develop a method for model selection for any given test event. These ideas are both new. They lead to developing models that are more accurate and also more robust. Approach 2 also has fundamental differences compared to the method in [43], where the introduction of Λ as a new feature has led to significant performance improvements. We also propose two new methods to use synchronized waveform measurements from multiple IBRs to reuse an existing model to predict the dynamic response of other IBRs to similar sub-cycle oscillations. These methods transfer a model that is *already trained* for one real-world IBR to another real-world IBR *without* the need to retrain the model for the new IBR. The second method is particularly novel as it eliminates the need to conduct an exhaustive search to select the model transfer parameter. Finally, the analyses in this journal version are based on a much larger dataset, with over twice the instances of real-world sub-cycle oscillatory events. Given the data-driven nature of this study, a much larger dataset is critical to provide a more in-depth understanding of the results.

Table I provides a comparison between the proposed approaches in this paper and comparable approaches in the literature. The first distinction is with respect to the type of data that is used for the analysis. Phasor-based methods are inherently incapable of addressing IBRs' sub-cycle dynamics because such dynamics are *not* visible in phasor measurements. As for methods that use waveform measurements, they can indeed model IBRs' sub-cycle dynamics. However, such literature has only recently begun to emerge. Compared to the few existing

TABLE I
SUMMARY OF COMPARABLE IBR MODELING APPROACHES.

Data	Methodology	References	No Prior Knowledge	Sub-cycle Dynamics	Captures Nonlinearity	Adaptive to Pre-Event Conditions	High Accuracy
Phasors	Physics-Based	[15][16]	×	-	-	-	-
	Data-Driven	[25][20]	✓	-		-	-
	Impedance-Based	[23]	✓	-	-	-	-
Waveforms	Multi-Model Linear Regression	[21]	✓	✓	×	×	×
	Nonlinear Neural Network Regression†	[22]	✓	✓	✓	×	×
	Proposed Approaches	-	✓	✓	✓	✓	✓

† Originally based on phasors, but it can be readily extended to waveforms.

Fig. 1. A WMU installation at an IBR: (left) a three-phase commercial PV inverter; (right) a WMU to record GPS time-stamped waveform measurements.

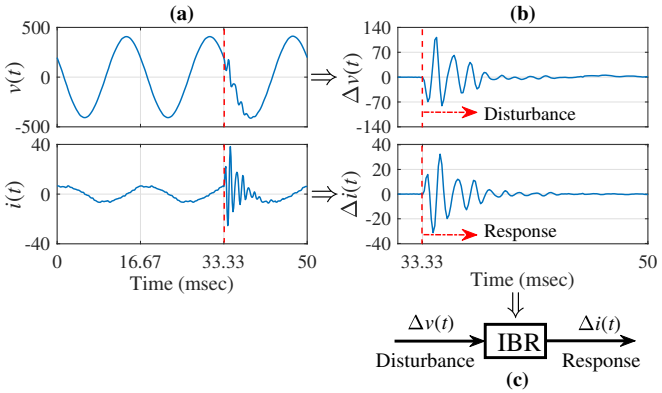

Fig. 2. (a) a sub-cycle voltage oscillation event, which causes agitation in the injected current by the IBR; (b) the corresponding differential waveforms that capture the signatures of the sub-cycle disturbance and the sub-cycle response of the IBR; (c) a data-driven model for the input-output relationship between the sub-cycle disturbance and the sub-cycle response of the IBR.

methods in this domain, our approaches address several gaps, such as the ability to capture nonlinear dynamics, the ability to adapt to pre-event conditions, and the ability to provide high-accuracy models for sub-cycle dynamics.

The findings in this paper are practical and can help utilities and system operators. For example, the proposed models can be used for condition monitoring and diagnostics at IBRs. This can directly help with safe and secure operation of IBRs, especially when it comes to GERs where utilities have limited observability. Apart from comparing the behavior of similar IBRs to identify abnormal dynamics, the proposed models can also detect any significant changes in the dynamic behavior of each IBR, indicating potential failures that may require site inspection. The proposed data-driven methods can also help developing digital twins for IBRs, to predict their responses to various power system disturbances, and to prevent undesirable tripping. Indeed, digital twins are being increasingly used in power networks and other cyber–physical systems for diverse applications; see [44]. Finally, the analysis in this paper can also be employed to compare the dynamic responses of IBRs in a region, to predict ripple effects, such as momentary IBR disruption, that may follow certain system-wide disturbances.

II. PROBLEM STATEMENT

Consider an IBR that is equipped with a WMU, such as the example in Fig. 1. The IBR in this figure is a commercial PV unit in Riverside, California. The WMU, which in this example is an SEL 735, measures both voltage and current waveforms. The voltage measurements indicate the IBR's terminal voltage on each phase. The current measurements indicate the IBR's injected current on each phase. The waveform measurements are precisely time-stamped by using an on-site GPS receiver.

The IBRs in this study were monitored continuously for an entire year. Every sub-cycle oscillatory disturbance was recorded during this period. These disturbances occurred at various times of the day, at different solar power production levels, and at different terminal voltage levels. As a result, the sub-cycle oscillatory events were captured under a wide range of operating conditions. The IBRs' control behavior was also affected by these changes in the operating conditions. In fact, the importance of considering the pre-event conditions in the proposed models, which is a major contribution of this paper, stems from the diversity of the operating conditions and their impact on the behavior and control dynamics of the IBRs.

Next, consider the *real-world* waveform measurements in Fig. 2(a) recorded by the WMU during a system-wide disturbance. Only one phase is shown here. The voltage and current waveform measurements are denoted by $v(t)$ and $i(t)$, respectively. A disturbance in the power system causes a *momentary voltage oscillation event* at the location of the PV inverter that lasts only about half of an AC cycle. The change in voltage causes a *dynamic response* in the PV inverter's current waveforms, which are transient and oscillatory. Our goal is to model this dynamic response at the *waveform level*, relying solely on data-driven methods based on the waveform measurements at the IBR, without requiring access to the internal physical models of the IBR components.

Next, consider Fig. 2(b). It shows the *differential waveforms* corresponding to the original voltage and current waveform measurements that we mentioned in the previous paragraph. Given a waveform measurement $x(t)$, its corresponding differential waveform $\Delta x(t)$ is defined as the difference between $x(t)$ and a *delayed version* of $x(t)$. Mathematically, the

differential waveform can be expressed as [45, Section 4.2.5]:

$$\Delta x(t) = x(t) - x(t-T), \quad \forall\, t \geq t_0, \tag{1}$$

where t_0 is the moment of the start of the event and $T = 1/60$ seconds denotes the waveform interval. Compared with the raw waveforms in Fig. 2(a), the differential waveforms in Fig. 2(b) provide a clearer signature of the sub-cycle disturbance and a clearer signature of the sub-cycle response of the IBR.

It is worth mentioning that, while both voltage and current waveforms in Fig. 2(a) are *sinusoidal* during the *steady-state* conditions *before* the event, the steady-state current waveforms are *more distorted* than the steady-state voltage waveforms. The level of steady-state harmonic distortions in the IBR's injected current can vary across different real-world IBRs, depending on their make, model, age, and various operating conditions. Notably, the steady-state distortions *before* the start of the event are mostly *canceled out* when we derive the differential waveforms to extract the event signature, as it is evident in the well-shaped voltage and current differential waveforms in Fig. 2(b), both of which clearly show the sub-cycle event signatures despite the higher steady-state harmonic distortion in the current waveforms prior to the event.

Finally, consider Fig. 2(c). It shows the input-output relationship between the differential waveform signatures of the sub-cycle disturbance and the differential waveform signatures of the sub-cycle response of the IBR:

$$\begin{aligned} &\text{Input Time-Series:} \quad \Delta v(t), \\ &\text{Output Time-Series:} \quad \Delta i(t). \end{aligned} \tag{2}$$

Fig. 3 shows the relationship between each sample of the differential voltage waveform (the input) and the corresponding sample of the differential current waveform (the output). Let $\Delta v[k]$ denote measurement sample k of the voltage differential waveform, and $\Delta i[k]$ denote measurement sample k of the current differential waveform. When there is no event, we have $\Delta v[k] \approx 0$ and $\Delta i[k] \approx 0$ for any k. Thus, in the absence of an event, we see only a single point at the origin, in the middle of the figure. Once an event occurs, it creates a non-zero sample $\Delta v[k]$ in the differential voltage, which has a corresponding non-zero sample $\Delta i[k]$ in the differential current. Thus, plotting $\Delta v[k]$ versus $\Delta i[k]$ at each sample k demonstrates the relationship between the event and the response of the IBR for each sample k. This results in a scatter plot, similar to the one in Fig. 3, where most points are away from the origin due to the impact of the event. If the relationship between differential current and differential voltage were linear, then the points would approximately form a line. However, since the relationship is nonlinear, the points are widely scattered, which is the case in Fig. 3.

Modeling such complex dynamics solely based on measurements, without access to the physical models of the internal elements of the IBRs, is a very challenging task. Next, we discuss our proposed methods to tackle this open problem.

III. Approach 1: Basic LSTM Model

In this section, we introduce our first model based on LSTM. We will enhance this model based on new features and methods in Sections IV and V. The step-by-step process in this paper to improve the models provides an in-depth understanding of why and to what extent each technical enhancement results in further improvements in model accuracy.

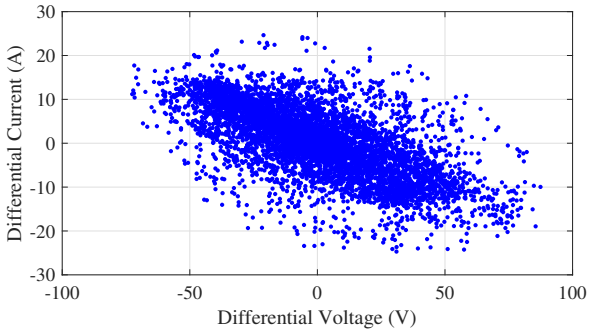

Fig. 3. The relationship between each sample of the differential voltage waveform and the corresponding sample of the differential current waveform at an IBR during several sub-cycle oscillatory disturbances.

A. LSTM Architecture and Methodology for Approach 1

Fig. 4 illustrates the overall architecture of the proposed model in Approach 1. The input to this model is a window of length *lag* of the most recent samples of the time series of the differential voltage waveform. The output of this model is the present sample of the time series of the differential current waveform. Note that, while notations $\Delta v(t)$ and $\Delta i(t)$ in (2) denote the entire time series of the differential waveform measurements, notations $\Delta v[t]$ and $\Delta i[t]$ denote the samples of these two time series at any given time t. If there are N samples in the differential voltage and the differential current, then there will be N windows of length *lag*, traversing the input signal, sample by sample, from left to right, in order to reconstruct the entire current waveform response of the IBR.

The main objective of the model in Approach 1 is to discern the relationship between each window of the most recent samples in the input time series and its corresponding output. This relationship can be expressed as follows:

$$\Delta i[t] \;=\; f\big(\Delta v[t],\, \Delta v[t-1],\, ...,\, \Delta v[t+1-lag]\big) \tag{3}$$

where we seek to identify the optimal choice of function $f(\cdot)$.

It is worth noting that, prior to constructing the windows of the input signal, the event data is partitioned into two sets: *training* events and *test* events. Following the construction of the input windows for all training events, the windows, along with their corresponding outputs, are *shuffled* and further *split* into training and validation data. This process guarantees a diverse representation of the dynamics of the system across different events, in both training and validation datasets.

The proposed model in Fig. 4 incorporates two LSTM layers to enable capturing the temporal dependencies within the sequential data. The core components of each LSTM cell include three gating mechanisms [26]: the input gate, the forget gate, and the output gate, as shown below, respectively:

$$\begin{aligned} i[t] &= \sigma(W_{ii}x[t] + b_{ii} + W_{hi}h[t-1] + b_{hi}), \\ f[t] &= \sigma(W_{if}x[t] + b_{if} + W_{hf}h[t-1] + b_{hf}), \\ o[t] &= \sigma(W_{io}x[t] + b_{io} + W_{ho}h[t-1] + b_{ho}), \end{aligned} \tag{4}$$

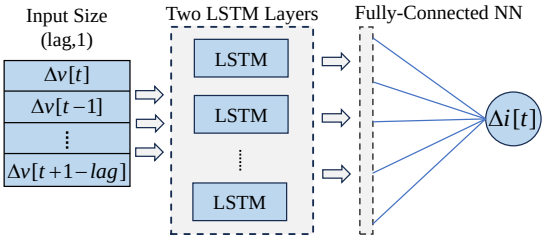

Fig. 4. Architecture of the proposed model in Approach 1.

where x_t is the input at time t and $h[t-1]$ is the hidden state from the previous time step. The weight matrices W and bias vectors b are parameters that are learned during the training process. The gates in (4) are controlled by sigmoid activation functions $\sigma(\cdot)$, which generate values between 0 and 1, determining the flow of information through the cell. A *tanh* activation function is applied to the candidate cell state:

$$g[t] = \tanh(W_{ig}x[t] + b_{ig} + W_{hg}h[t-1] + b_{hg}), \quad (5)$$

allowing the model to capture long-term dependencies. The cell state that represents the long-term memory is modified by the input gate, forget gate, and candidate cell state as

$$c[t] = f[t]c[t-1] + i[t]g[t]. \quad (6)$$

The hidden state that serves as the short-term memory is calculated using the output gate and the current cell state as:

$$h[t] = o[t]\tanh(c[t]) \quad (7)$$

Subsequently, a layer of a fully connected neural network serves as the last layer of the network architecture in Fig. 4, generating the ultimate output of the network.

In Approach 1, hyperparameters were set manually to commonly used values. The LSTM layers have 64 units. The activation function is $tanh$, chosen for its ability to model complex and nonlinear relationships. Two Dropout layers, each with a dropout rate of 0.3, follow the LSTM layers, mitigating overfitting by randomly deactivating a fraction of neurons during training. The final Dense layer with 1 unit and a ReLU activation function produces the output. The model is trained using Adam optimizer (learning rate of 0.01) over the MSE loss function. Thirty percent of the training data is used for validation. TensorFlow's Keras API was used to build the LSTM network, with its default random weight initialization.

B. Experimental Results and Performance Comparison

In this section, we compare Approach 1 with two methods in the literature, namely Multi-Model Linear Regression [21, Section IV] and Nonlinear Neural Network Regression [22]. To have a fair comparison, we use the exact same real-world training and testing data for all methods. Specifically, we use waveform measurements from a WMU at a 480 V/100 kW PV unit over one year. The WMU is an "event-triggered" device, where it records the waveform measurements only if an event occurs. The vast majority of the events that are recorded by the WMU are typical power quality disturbances such as voltage sags. However, this study only uses the

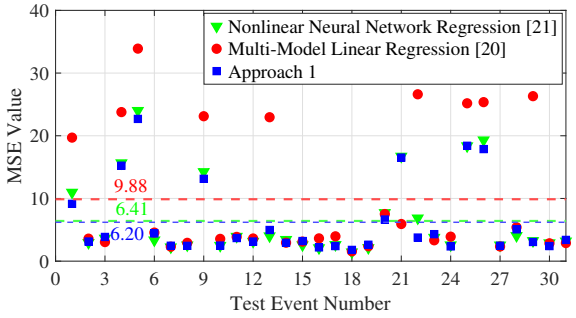

Fig. 5. Individual MSE values (and their averages in the dashed lines) for all the Test Events, for the proposed model in Approach 1, in comparison with the methods based on regression analysis in [21] and [22].

event-triggered waveform measurements that involved sub-cycle disturbances. Importantly, such sub-cycle disturbances cannot be captured by other sensor technologies such as PMUs. The measurements from the WMU are collected by using the SynchroWave software [46], in COMTRADE or CSV format, and stored on a Google Cloud Platform (GCP). A total of 147 sub-cycle oscillatory disturbances and the corresponding dynamic responses of the IBR to these 147 disturbances were analyzed. Unless stated otherwise, we allocate 116 disturbances ($\sim$ 80%) for training and 31 disturbances ($\sim$ 20%) for testing. The dominant frequency of the sub-cycle oscillations in our dataset varies between 590 Hz and 874 Hz. Each event also includes several other frequency components. For example, the voltage oscillation in Fig. 2 comprises considerable oscillatory modes at 768 Hz, 853 Hz, 682 Hz, and 1109 Hz, where the frequency of the dominant oscillatory mode (i.e., the dominant frequency) is 768 Hz. Such diverse presence of oscillatory modes (both dominant and otherwise), creates a highly challenging real-world dataset for the purpose of our performance evaluation.

The randomness inherent in the training process of the model is addressed by conducting 40 iterations of training. This helps mitigate the influence of stochastic variations, ensuring a more robust and representative analysis. Therefore, all the results presented in this paper are derived from the average outcomes obtained over these 40 training iterations.

Fig. 5 shows the results. The individual points with markers show the average MSE for each of the 31 test cases for each method. The dashed lines show the *average* Mean Squared Error (MSE). The average MSE for the Multi-Model Linear Regression method in [21] is 9.88, and for the Nonlinear Neural Network Regression method in [22] is 6.41. Approach 1 reduces the average MSE to 6.2. This indicates a 37% and a 3% improvement in modeling accuracy, compared to the methods in [21] and [22], respectively. Notably, the Nonlinear Neural Network Regression method outperforms the Multi-Model Linear Regression method due to its ability to capture nonlinear patterns in the IBR dynamics.

IV. Approach 2: Enhanced Model with Additional Features and Additional Layer

While Approach 1 demonstrated an improvement compared to the methods in the literature, there was a considerable

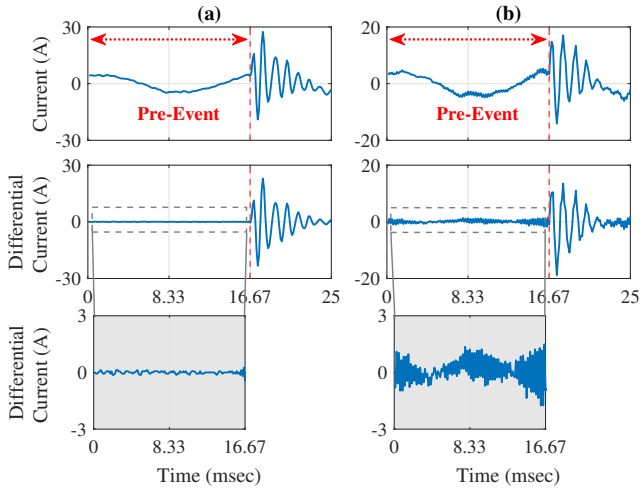

Fig. 6. Examples of different pre-event conditions: (a) a response with a stable pre-event condition; (b) a response with high-frequency pre-event fluctuations.

number of test cases in Fig. 5 that had very high MSE values, as high as 20. Upon further examination, we observed some test cases that had *almost identical* differential voltage waveforms (i.e., inputs), yet they showed *significant differences* in their differential current waveforms (i.e., outputs). Therefore, it appeared that at least one cause for the poor performance of Approach 1 in some of the test cases is the lack of incorporating the IBR's *pre-event operating conditions* in the model. Accordingly, in this section, we introduce a new design that can address this shortcoming to further improve the performance of the initial method in Approach 1.

A. New Features to Incorporate Pre-Event Conditions

To incorporate the pre-event operating conditions of the IBR, we examined the characteristics of the differential current waveform at the cycle *immediately before* the start of the event. Recall from Section II that the start time of an event is denoted by t_0 and the period of each cycle is denoted by T. Accordingly, the differential current waveform in the cycle immediately before the start of the event can be obtained as

$$\Delta i[t_0 - T - 1 : t_0 - 1]. \tag{8}$$

Next, we introduce two new features based on the expression in (8). These two features can capture the *pre-event conditions* of the IBR when it dynamically responds to each disturbance. The first new feature is defined as follows:

$$\Gamma = \|\Delta i[t_0 - T - 1 : t_0 - 1]\|_2. \tag{9}$$

If Γ = 0, then the IBR was in a truly steady-state condition when the event happened. On the other hand, a large Γ indicates that the pre-event condition at the IBR was far from steady-state, such as due to a recent event that is still affecting the behavior of the IBR, or due to an internal dynamic in the IBR that has not reached steady-state condition yet.

The second new feature is defined as follows:

$$\Lambda = \arg\max_{f} \ \text{FFT}\left\{\Delta i[t_0 - T - 1 : t_0 - 1]\right\}, \tag{10}$$

where FFT$\{\cdot\}$ denotes the Fast Fourier Transform of the differential current waveform in (8). The maximization in (10) is across the frequency modes that are present in the FFT. In other words, Λ is the dominant frequency component in the pre-event differential current of the IBR. A higher Λ indicates the presence of transient high-frequency oscillations in the IBR's injected current at the time that the disturbance occurs in the power system. This feature should be extracted based on the steady-state condition when the event occurs. Therefore, if there is an event preceding the event for which we calculate Λ, we may consider at least two cycles before the start of the event to ensure that the system is in a steady state situation.

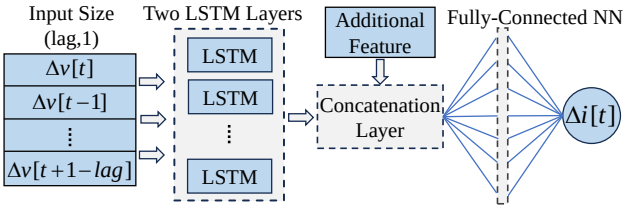

Fig. 7. Architecture of the proposed model with an additional layer.

For example, consider the two current waveforms in Figs. 6(a) and (b) that belong to two different events. The pre-event cycle is marked on both figures with the double-sided arrows. The corresponding differential waveforms are also shown in each case. Notice the significant high-frequency oscillations in the event in Fig. 6(b). This is particularly visible when we zoom in on the differential waveform during the pre-event cycle. We have Λ = 960 Hz for the event in Fig. 6(a), and Λ = 3780 Hz for the event in Fig. 6(b).

Additional information, such as the RMS value of the IBR's terminal voltage, denoted by V_{RMS}, or the RMS value of the IBR's injected current, denoted by I_{RMS}, may also serve as additional features with regards to the IBR's operating conditions. However, as we will see in our experimental results in Section IV-C, adding features Γ and Λ is significantly more efficient than adding V_{RMS} and I_{RMS} as features.

B. LSTM Model with an Additional Feature Layer

While $\Delta v(t)$ and $\Delta i(t)$ are time series, the new features in Section IV-A are *scalars*. To incorporate them into the model, we propose to add a new *concatenation layer* between the second LSTM layer and the final layer of the fully-connected neural network. Accordingly, we propose a new architecture, as in Fig. 7. Based on this new architecture, each time series of the differential voltage is assigned a label by the additional layer. This label represents one of the new scalar features, serving as a novel input to the model. Therefore, the original objective of the LSTM model in (3) can be reformulated as follows to align with the new architecture:

$$\Delta i[t] = f(\Delta v[t], \Delta v[t-1], ..., \Delta v[t+1-\text{lag}], F), \tag{11}$$

where F is a new input to the model, representing one of the new scalar features that we introduced in Section IV-A.

The parameters in Approach 2 are mostly similar to Approach 1, except for the new concatenation layer. The input size to this new layer is equal to the output size of the second LSTM layer *plus one*, and its output size is equal to the input size of the last layer. This new layer has 64 units and employs ReLU activation function to process the combined information.

TABLE II
AVERAGE MSE BASED ON THE NEW ARCHITECTURE WITH AN ADDITIONAL LAYER

Feature	Γ	Λ	V_{RMS}	I_{RMS}
Average MSE	**2.07**	**1.96**	6.51	5.54

C. Experimental Results and Performance Comparison

Table II shows the average MSE for the 31 Test events when employing the proposed model in Approach 2. The results indicate a *drastic enhancement* in model accuracy with the incorporation of an additional layer to include Γ or Λ. There are also *some* (albeit minor) improvements when I_{RMS} is used as new features. As for adding V_{RMS} as a new feature, it appears to slightly degrade the performance. It should be noted that, while features Γ, Λ, and I_{RMS} are based on the IBR's pre-event operating conditions, feature V_{RMS} is based on the power network's (i.e., the grid's) pre-event operating conditions.

In summary, by revising the architecture and incorporating the IBR's pre-event conditions through features Γ and Λ, we achieve 67% and 68% improvement in the model accuracy in Approach 2 compared to Approach 1, respectively.

V. Approach 3: Constructing Multiple Models with Model Selection

In this section, we propose another method to further improve accuracy. We divide the training dataset into two or more *clusters* based on a similarity index. Each cluster is then used to develop a separate model. For each test event, we use the same similarity index to identify which model should be used to best capture the dynamics of the IBR during that test event.

A. Construction of Clusters and Models

Without loss of generality, we assume that the number of clusters is two, i.e., the training dataset is divided into two clusters. The metric for clustering, i.e., the similarity index, can be any feature that is used in the analysis of the waveform measurements. For example, if we seek to cluster the training events based on the IBR's pre-event operating conditions, then we can use one of the features that we defined in Section IV-A, as the metric for clustering. Let F denote the feature that serves as the metric to assess similarity among the training events for the purpose of clustering. Let F_i denote the value of this feature for training event i. Let b_i denote a binary variable, which is 1 if we place training event i in the first cluster, and it is 0 if we place training event i in the second cluster. Clustering can be done by using k-means clustering [47], i.e., by minimizing the within-cluster sum-of-squares:

$$\min_{\mathbf{b}} \quad \sum_i ||b_i F_i - \mathbf{b}^T\mathbf{F}/\mathbf{1}^T\mathbf{b}||^2 + \sum_i ||(1-b_i)F_i - (\mathbf{1}-\mathbf{b})^T\mathbf{F}/\mathbf{1}^T(\mathbf{1}-\mathbf{b})||^2, \tag{12}$$

where $\mathbf{F}$ is the vector that contains F_i for all training events, $\mathbf{b}$ is the vector that contains b_i for all training events, and $\mathbf{1}$ is a vector of ones which has the same length. Notice that $\mathbf{b}^T\mathbf{F}/\mathbf{1}^T\mathbf{b}$ is the average of feature F among the training events in the first cluster, and $(\mathbf{1}-\mathbf{b})^T\mathbf{F}\ /\ \mathbf{1}^T(\mathbf{1}-\mathbf{b})$ is the average of F among the training events in the second cluster.

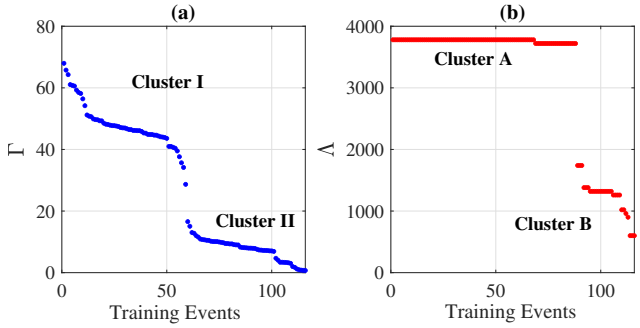

Fig. 8. The values of Γ and Λ, sorted by magnitude, for all the 116 events in the training data set. Both features can naturally result in dividing the training events into two clusters (but different clustering).

Accordingly, we can use either Approach 1 in Section III or Approach 2 from Section IV to construct two models:

- Model 1 based on Training Data in Cluster 1,
- Model 2 based on Training Data in Cluster 2.

B. Model Selection

If a test event is similar to the training events in Cluster 1 then Model 1 is a better choice to capture its dynamics. If a test event is similar to the training events in Cluster 2 then Model 2 is a better choice to capture its dynamics. Let F_{Test} denote the value of feature F for a test event. We can compare the following two expressions to assess the similarity of the test event with the training events in the two clusters:

$$||F_{\text{Test}} - \mathbf{b}^T\mathbf{F}/\mathbf{1}^T\mathbf{b}||^2 \tag{13}$$

and

$$||F_{\text{Test}} - (\mathbf{1}-\mathbf{b})^T\mathbf{F}/\mathbf{1}^T(\mathbf{1}-\mathbf{b})||^2. \tag{14}$$

That is, if (13) is less than or equal to (14), then we use Model 1 to predict the output of the IBR to the disturbance in the given test event. Otherwise, we use Model 2.

C. Experimental Results and Performance Comparison

Recall from Table II in Section IV that feature Γ in (9) and feature Λ in (10) are the most effective features to capture the IBR's pre-event operating conditions. Accordingly, either one can be a good candidate as the metric for clustering the training data. This is show in Fig. 8. We show both features across all the 116 training events, sorted in a descending order. Notably, both features result in some obvious clustering among the training events. In both cases, a simple threshold can separate the two clusters. For example, we can group the training events with $\Gamma \geq 20$ into Cluster I and the training events with $\Gamma < 20$ into Cluster II; see Fig. 8(a). Furthermore, we can group the training events with $\Lambda \geq 2500$ into Cluster A and the training events with $\Lambda < 2500$ into Cluster B; see Fig. 8(b).

Importantly, Cluster I and Cluster II are *not* the same as Cluster A and Cluster B. This can be understood by calculating the Adjusted Rand Index (ARI) between the two clustering results, which is a number between -1 and 1:

$$\text{ARI(Clusters I and II, Clusters A and B)} = -0.0038 \tag{15}$$

A small ARI, including a negative ARI, indicates that clustering is done differently by the two methods [48]. From (15), it

TABLE III
AVERAGE MSE FOR DIFFERENT METHODS

Method	Average MSE
Multi-Model Linear Regression [21]	9.88
Nonlinear Neural Network Regression [22]	6.41
Approach 1	6.20
Approach 2 - Γ as Input	2.07
Approach 2 - Λ as Input	1.96
Approach 3 - Λ as Input - Γ for Clustering	**1.80**
Approach 3 - Γ as Input - Λ for Clustering	**1.61**

is clear that a clustering based on Γ and a clustering based on Λ are different. Nevertheless, they both result in improvements in the accuracy of the model, as we will discuss next.

From the above results, two clusters appear to be sufficient for the events in our real-world dataset. However, this number could be specific to this dataset. Other real-world datasets may require using more clusters. The exact number of clusters is determined based on the training data, similar to the analysis in Fig. 8. Therefore, while the methodology in Approach 3 *can* be generalized, the conclusion about the sufficient number of clusters may *not* necessarily be generalized to other datasets.

Table III shows the average MSE for different methods. The last two rows are of particular interest. Notice that Approach 3 results in additional improvements compared to Approach 2, regardless of the choice of feature that is used for clustering. The best result in Approach 3 is achieved when we use Λ for clustering and model selection, while using Γ as input for the additional layer. This strategy is further supported by the distributions of features Λ and Γ, as depicted in Fig. 8. The distribution of Λ exhibits a binary-like pattern while the distribution of Γ spans a broad range of values, from 70 to 0.

The MSE values for each test case are shown in Fig. 9. Here, we compare the best strategies from Approach 3 (Γ as input and Λ for clustering) and Approach 2 (Λ as input). Approach 3 outperforms Approach 2 in most test cases.

D. Computation Time

Recall from Section III that all waveform measurements are collected and stored on GCP. Accordingly, all computations are also performed directly on Google Colab within GCP. The proposed models are trained on a GCP virtual machine with the following default setting: *n1-standard-96* machine type, which includes 96 virtual CPUs, four NVIDIA Tesla T4 GPUs, and 16 GB of memory. We did not modify these default parameters. The results for the computational runtime

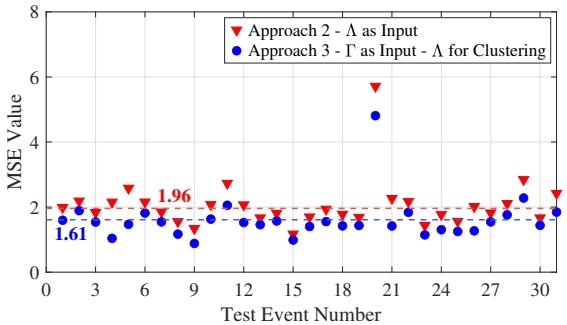

Fig. 9. Individual MSE values (and their averages in the dashed lines) for the proposed models in Approach 2 and Approach 3.

TABLE IV
RUNTIMES IN SECONDS

Model	**Training (50 Epochs)**	**Testing (Per Test Event)**
Multi-Model Linear Regression	2.1	0.07
Nonlinear Neural Network Regression	16.42	0.09
Approach 1	40.27	0.10
Approach 2	47.84	0.11
Approach 3	56.26	0.11

TABLE V
MODEL ACCURACY FOR DIFFERENT PERCENTAGES OF TRAINING DATA

Percentage of Training Aata	20%	40%	60%	80%
MSE	5.41	3.08	2.00	1.86

(in seconds) are presented in Table IV.

We distinguish between the computational complexity of the training phase versus the testing phase. Training is typically a one-time task. Thus, longer computational times are generally not a concern. Nevertheless, even for training, the runtime remains under one minute. Testing and inference, in contrast, are more time-sensitive. However, once the models are trained, testing is efficient and lightweight. The runtime for testing is only a small fraction of a second, as shown in Table IV.

E. Sensitivity to Size of Training Data

Table V shows the model accuracy for different percentages of training data. The results are for Approach 3, the version where Γ is an input and Λ is used for clustering, i.e., the approach with the best performance. We can make three observations in Table V. First, increasing the percentage of training data improves model accuracy. For instance, there is a substantial performance improvement when we increase the training data from 20% to 40%. Second, the performance is already desirable even at 60% training data, since the MSE in this case is only slightly greater than the MSE under 80% training data. Third, with only 20% training data, the MSE in Table V for Approach 3 is less than the MSE in Table III for Multi-Model Linear Regression, Nonlinear Neural Network Regression, and Approach 1, all of which use 100% of training data. This is a clear indication of the superior performance of Approach 3 even with much lower training data.

F. Sensitivity to Hyperparameters

In this section, we conduct a sensitivity analysis to investigate the impact of changing the key hyperparameters on the performance of proposed methodologies. The results are shown in Table VI, with respect to the number of hidden units

TABLE VI
SENSITIVITY TO HYPERPARAMETERS

Parameter	Number of Hidden Units per Layer			Dropout Rate		
Value	32	64	128	0.2	0.3	0.4
MSE	1.73	1.61	1.65	1.61	1.75	1.79

Parameter	Learning Rate		Batch Size		
value	0.001	0.01	32	64	128
MSE	1.60	1.61	1.71	1.64	1.61

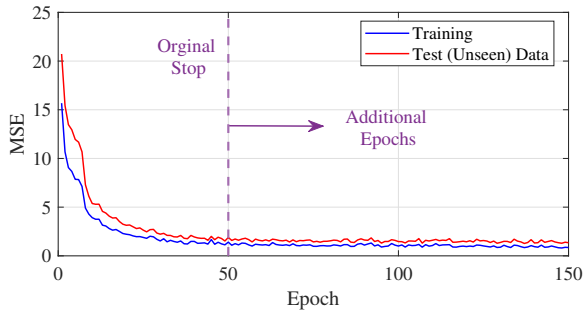

Fig. 10. An experiment to check for over-fitting. MSE for Approach 3 is plotted at each epoch, based on training data and also based on test data. Both curves follow the same trend, suggesting that over-fitting does not occur.

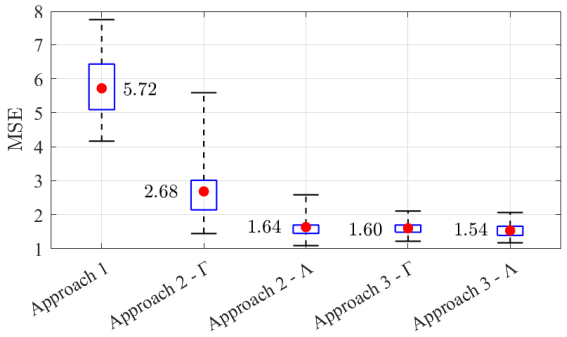

Fig. 11. Distribution of MSE over 50 different random training event selection scenarios. The black box represents the interquartile range, the whiskers indicate the minimum and maximum, and the red dot marks the mean.

in each layer, the dropout rate, the learning rate, and the batch size. The results are based on Approach 3. As we can see, the changes in these hyperparameters affect the MSE values only slightly. Overall, the model demonstrates robust performance under varying reasonable hyperparameters.

G. Checking for Possible Overfitting

Overfitting is a major concern in training neural networks. It occurs when a model performs very well on training data but generalizes poorly to unseen data [49]. To assess the potential for overfitting, we must compare the training loss with the loss of unseen test data over epochs [49]. If the loss for the unseen test data *decreases along with* the training loss, then it suggests good generalization. If the loss for the unseen test data *starts increasing* while the training loss continues decreasing, then it raises concerns about potential overfitting in the model.

The above analysis is shown in Fig. 10. Here, we calculate two MSE values at the end of each epoch. One MSE value is calculated based on the training data, while the other is calculated based on the test data. All the results so far are based on 50 epochs for training. However, to check for overfitting, we increased the number of epochs by three-fold, to 150 epochs. This was done to determine whether the MSE for the unseen test data would eventually increase, which could suggest over-fitting. Notably, the test data remains unseen throughout the process, i.e., the test data does *not* influence the training process in any way. The test data is used solely for performance evaluation at the end of each epoch.

As we can see in Fig. 10, both the training MSE and the testing MSE continue to gradually decrease as the number of epochs increases. Therefore, it is evident that overfitting does *not* occur in the analysis presented in this paper.

H. Random Scenarios

Next, we further examine the performance of the proposed models based on various choices of training and test events. We first randomly select a subset of the events as training data. The remaining events are used as test data. This process is then repeated 50 times to generate 50 random scenarios to ensure conducting a comprehensive assessment. Same as before, the number of events in the training dataset is 116 (i.e., 80%) and the number of events in the test dataset is 31 (i.e., 20%).

Fig. 11 shows the distribution of the results, including the mean, the minimum, the maximum, and the interquartile range. The interquartile range indicates the 25th and 75th percentiles. The results in Fig. 11 are consistent with the results in Table III, further confirming the step-by-step improvements across the methods, and the more robust performance of the results in Approach 3. Notice that Approach 3 exhibits lower variance across different test scenarios. Furthermore, Approach 3 shows reduced sensitivity to changing the features, suggesting a more stable and adaptable modeling methodology.

I. Assessment based on Simulation Data

All the results in this paper are based on real-world data. However, it is insightful to also explore the results when the data are generated by computer simulation. We used the IBR model in [50], which was developed in PSCAD. PSCAD is a proper tool for voltage and current waveform simulation of IBRs because it provides high-fidelity waveform modeling, enabling the representation of sub-cycle dynamics, power electronics behavior, and control interactions in IBRs.

For a comparable analysis, we used the real-world voltage waveform measurements in our dataset as the terminal voltages for the simulated IBR model. We then recorded the simulated injected current of the IBR model in PSCAD. Accordingly, the inputs to the simulated IBR model resemble those in the real-world measurements, while the outputs differ since they are based on computer simulations of the IBR.

The results are shown in Fig. 12. First, consider the waveforms in Fig. 12(a). It shows an example waveform response of the simulated IBR model to a real-world disturbance in voltage waveform. Notice that the IBR's response in this figure is generally similar to the various responses presented throughout this paper, suggesting that the simulated IBR model is generally reliable for capturing sub-cycle dynamics.

Next, consider the MSE values in Fig. 12(b). They are obtained based on the same 50 random scenarios that we use in Section V-H. In the chart on the left, both training and testing are performed using real-world data. In the chart on the right, both training and testing are performed using simulated data. All the results in both charts in this figure are based on Approach 1. It is evident from Fig. 12(b) that the proposed method performs very well on simulated data. In fact, performance is significantly better for the simulated data than for real-world data, with the average MSE decreasing from 5.72 to 3.51. This improvement is likely due to the

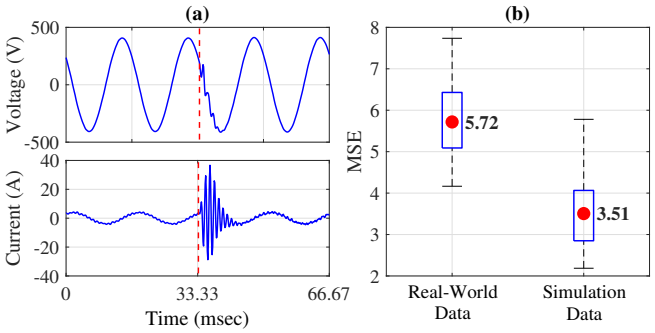

Fig. 12. Results from computer simulations: (a) The response of a simulated IBR model to a real-world disturbance; (b) The performance of Approach 1 across 50 random scenarios based on real-world Data and simulation Data.

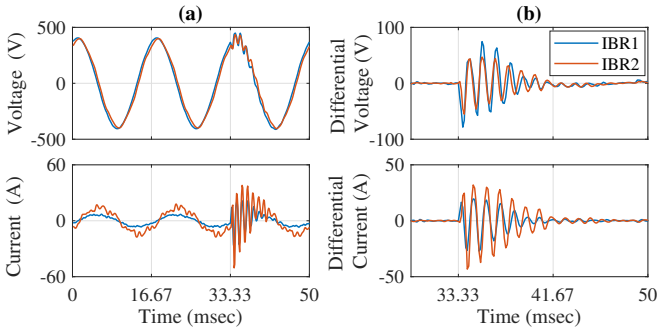

Fig. 13. Time-synchronized waveform measurements at two different IBRs during the same sub-cycle voltage oscillation disturbance: (a) the raw waveform measurements; (b) the corresponding differential waveforms.

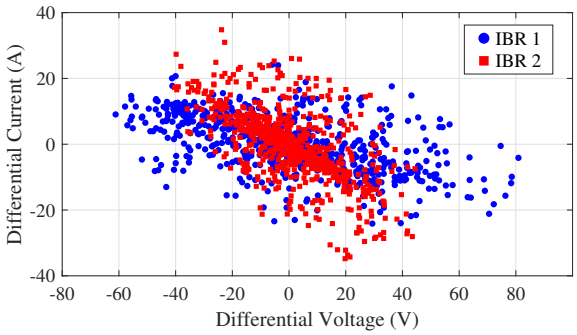

Fig. 14. The relationship between each sample of $\Delta v(t)$ and the corresponding sample of $\Delta i(t)$, for IBR 1 and IBR 2, based on their responses to the events that are simultaneously captured by *both* WMU 1 and WMU 2.

lower complexity of the simulation model compared to real-world data, which is influenced by factors such as unmodeled dynamics and measurement noise. In summary, the proposed methods perform well on both simulated and real-world data.

VI. Using Synchro-waveforms to Model the Dynamic Response of Multiple IBRs

For the analysis in this section, we installed a second WMU to take advantage of the availability of *time-synchronized* waveform measurements. The two WMUs are located on two different 12.47 kV power distribution feeders. They are both installed at 480 V. The upstream transformers at each WMU location include 480 V to 12.47 kV and 12.47 kV to 69 kV. The 69 kV sides of the latter transformers are part of the same sub-transmission network. Thus, the electrical spread between the two WMU locations occurs at 69 kV. IBR 2 is made by the same manufacturer as IBR 1. However, it has a larger rated power and it is connected to a larger array of solar panels.

Accordingly, we were able to observe how the two IBRs *simultaneously* respond to the *same* sub-cycle voltage oscillation events. An example is shown in Fig. 13(a), where we plotted the *time-synchronized* raw voltage and raw current waveforms at the two IBRs. The voltage events are very similar at the two IBRs. In other words, the disturbance appears similarly at the two locations. As for the dynamic response of the IBRs, which are manifested in their current waveforms, they are generally similar except for their magnitudes. Another observation in Fig. 13(a) is the presence of higher distortions in the current waveforms at IBR 2 in the cycles before the start of the event.

Fig. 13(b) shows the differential waveforms corresponding to the same time-synchronized raw waveforms in Fig. 13(a). Again, the two IBRs' responses to the same disturbance are generally similar, but they have different magnitudes.

Next, consider the two scatter plots in Fig. 14. The black and red markers represent the dynamic response of IBR 1 and IBR 2, respectively. The scatter plot in Fig. 14 is solely based on the events that are simultaneously captured by *both* WMU 1 and WMU 2, where WMU 1 is installed at IBR 1 and WMU 2 is installed at IBR 2. Recall from Section II that this type of scatter plot illustrates the relationships between the samples of $\Delta v(t)$ (the input) and the corresponding samples of $\Delta i(t)$ (the output). The analysis in Fig. 14 shows the major differences between IBR 1 and IBR 2 in terms of their dynamic response to the *same* system-wide events. Evidently, the dynamic behaviors of the two IBRs exhibit some differences even in response to identical events. This raises a question: to what extent a model that is developed for one IBR can be used to capture the dynamic behaviour of another IBR, even if the two IBRs are made by the same manufacturer?

In this section, we explore two options to use an existing model that is trained for IBR 1 to predict the dynamic response of IBR 2 to similar sub-cycle oscillatory events.

A. Reusing IBR 1's Model without Additional Measurements

Let $f_{\text{IBR 1}}(\cdot)$ denote the model that is already trained for IBR 1. If we *reuse* this model to predict the dynamic response of IBR 2, then we can obtain the results as

$$\Delta i_{\text{IBR 2}}(t) = \lambda \times f_{\text{IBR 1}}\left(\Delta v_{\text{IBR 2}}(t)\right), \tag{16}$$

where λ is a *scaling factor*. It incorporates our previous observation that although the dynamics of IBR 1 and IBR 2 have some similarities they clearly have different magnitudes. If IBR 2 is larger than IBR 1, which is indeed the case for the two real-world IBRs in the study in this paper, then we set $\lambda > 1$. If IBR 2 is smaller than IBR 1, then we set $\lambda < 1$.

Fig. 15 shows the results for different choices of λ. Here, we apply the models from IBR 1 to predict the response of IBR 2 to the disturbances that are simultaneously captured at both IBR 1 and IBR 2. As we can see, a proper choice of λ can significantly improve MSE. In fact, whether we use Γ or Λ as the input feature, the most suitable λ is the same, at $\lambda = 1.8$. The minimum MSE is 10.76 if we use Γ as the input feature and 8.12 if we use Λ as the input feature. These are surprisingly high accuracy, given the fact that the model was

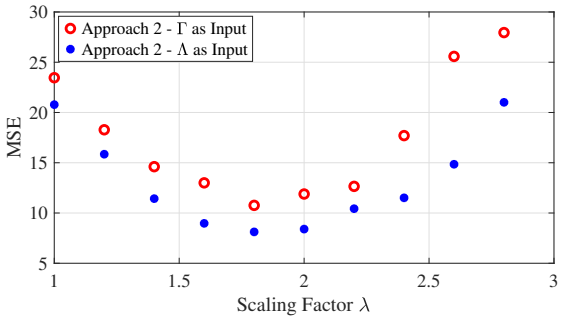

Fig. 15. The results for reusing the model from IBR 1 to predict the dynamic response of IBR 2. Regardless of whether we use Γ or Λ as the input feature to the model, the lowest MSE is achieved at the same λ.

developed based on the data from IBR 1, yet it was applied nicely to the data from IBR 2 with a very minor change.

Note that the unit of Γ is Amp. It depends on the size of the IBR. The unit of Λ is Hz. It does not depend on the size of the IBR. Thus, no adjustment was needed for Λ.

B. Adjusting IBR 1's Model Using Synchro-waveforms

The challenge with the method in Section VI-A is that we need to find a proper choice for the scaling factor. For instance, in Fig. 15, we had to do an exhaustive search and try several choices of λ to find the optimal choice of λ that could minimize the MSE for IBR 2. In fact, the right choice of λ may depend on not only the sizes of the IBRs but also the locations of the two IBRs on the power system.

Therefore, in this section, we use *synchro-waveforms*, i.e., time-synchronized waveform measurements, from IBR 1 and IBR 2 during *a few* disturbances that are captured at *both* IBR 1 and IBR 2 to properly scale the model from IBR 1 to be used for IBR 2 without the need to do an exhaustive search.

Suppose we have access to synchro-waveforms during N events that are captured at both IBRs. For each event $k = 1, \ldots, N$, the differential waveforms are obtained as follows:

$$\begin{aligned} &\text{IBR 1:} \quad \Delta v_{\text{IBR 1, } k}(t) \text{ and } \Delta i_{\text{IBR 1, } k}(t) \\ &\text{IBR 2:} \quad \Delta v_{\text{IBR 2, } k}(t) \text{ and } \Delta i_{\text{IBR 2, } k}(t). \end{aligned} \tag{17}$$

Let $V_{\text{IBR 1, } k}$ denote the magnitude of the dominant dynamic mode of $\Delta v_{\text{IBR 1, } k}(t)$, which can be obtained by applying Prony method to $\Delta v_{\text{IBR 1, } k}(t)$; see [45, p. 58]. Let us similarly define $I_{\text{IBR 1, } k}$, $V_{\text{IBR 2, } k}$, and $I_{\text{IBR 2, } k}$ based on the magnitude of the dominant mode of $\Delta i_{\text{IBR 1, } k}(t)$, $\Delta v_{\text{IBR 2, } k}(t)$, and $\Delta i_{\text{IBR 2, } k}(t)$, respectively. Hence, we can use the synchro-waveform measurements at IBR 1 and IBR 2 we obtain:

$$V_{\text{IBR 1, } k}, I_{\text{IBR 1, } k}, V_{\text{IBR 2, } k}, I_{\text{IBR 2, } k}, \quad k = 1, \ldots, N. \tag{18}$$

We must emphasize that N is a small number. For example, we may assume that a *mobile* WMU is *temporarily* installed at IBR 2 for a few hours to measure the voltage and current waveforms at IBR 2 during a handful of disturbances. In other words, N is *much smaller* than the number of waveform captures during disturbances that are necessary in order to train a new model for IBR 2; yet it is sufficient to let us quickly adjust the model from IBR 1 to be used for IBR 2.

TABLE VII
AVERAGE MSE FOR TWO METHODS THAT *Reuse* A TRAINED MODEL

Reusing Method	MSE	Exhaustive Search
Without Additional Measurements	8.12	On λ
With Additional Measurements (Using Synchro-waveforms)	7.89	-

Based on the available quantities in (18), we introduce:

$$\alpha = \frac{1}{N}\sum_{k=1}^{N} \frac{V_{\text{IBR 1, } k}}{V_{\text{IBR 2, } k}}, \quad \beta = \frac{1}{N}\sum_{k=1}^{N} \frac{I_{\text{IBR 2, } k}}{I_{\text{IBR 1, } k}}. \tag{19}$$

Notice that inverse form of the fractions in β versus in α.

Next, we propose to reuse the model from IBR 1 to predict the dynamic response of IBR 2 as follows:

$$\Delta i_{\text{IBR 2}}(t) = \beta \times f_{\text{IBR 1}}\left(\alpha \times \Delta v_{\text{IBR 2}}(t)\right). \tag{20}$$

To assess this method, we set $N = 6$. Accordingly, we obtain $\alpha = 1.49$ and $\beta = 1.34$. Upon applying the method in (20), the average MSE for the remainder of the events is obtained as 7.89, if we use Λ as the input feature. Table VII summarizes the results for both methods. There are two advantages to using the additional measurements. First, it eliminates the need to conduct an exhaustive search for λ or any other parameter. Second, it results in a lower MSE. Thus, it results in a model that is more accurate and more efficient.

VII. CONCLUSIONS

Three different data-driven approaches were proposed to use waveform measurements to model the dynamic behavior of IBRs in response to sub-cycle oscillatory disturbances. The performance of the proposed methods was evaluated using real-world GPS-synchronized waveform measurements. Approach 1 reduces the average modeling error by 37% and 3% compared to two recent methods in the literature: one based on multi-model (i.e., model-library) linear regression and one based on nonlinear neural network regression. The average modeling error further decreases by 68% in Approach 2. In Approach 3, the average modeling error decreases even further by another 18%. The high accuracy of the proposed methods is due to their ability to capture nonlinear dynamics, long temporal dependencies, and pre-event conditions. The latter aspect is particularly important in the superior performance of Approach 2 and Approach 3.

Furthermore, two new methods are proposed to *reuse* an existing model to predict the dynamic response of other IBRs to similar sub-cycle oscillations. Here, we transfer a model that is already trained for one real-world IBR to *another* real-world IBR *without* the need to retrain it for the new IBR. Both methods demonstrated good accuracy. However, the first method requires an exhaustive search to determine the optimal value of a transfer parameter, whereas the second method eliminates the need for such a search by using a few instances of time-synchronized waveform measurements.

REFERENCES

[1] W. Xu, Z. Huang, X. Xie, and C. Li, "Synchronized waveforms: A frontier of data-based power system and apparatus monitoring, protection, and control," *IEEE Trans. on Power Delivery*, vol. 37, pp. 3–17, 2022.

[2] H. Mohsenian-Rad and W. Xu, "Synchro-waveforms: A window to the future of power systems data analytics," *IEEE Power and Energy Magazine*, vol. 21, no. 5, pp. 68–77, Sep 2023.

[3] A. Silverstein and J. Follum, "High-resolution time-synchronized grid monitoring devices," NASPI Report NASPI-2020-TR-004, Mar. 2020.

[4] J. D. Follum, R. Hovsapian *et al.*, "Advanced measurements for resilient integration of inverter-based resources: Progress matrix year-1 report," Pacific Northwest National Laboratory (PNNL), Tech. Rep., 2023.

[5] North American Electric Reliability Corporation, "Multiple Solar PV Disturbances in CAISO," NERC Report, Apr. 2022.

[6] H. Mohsenzadeh-Yazdi, C. Li, and H. Mohsenian-Rad, "Ibr responses during a real-world system-wide disturbance: Synchro-waveform data analysis, pattern classification, and engineering implications," *IEEE Transactions on Smart Grid*, pp. 1–1, 2025.

[7] L. Fan, Z. Miao, and M. Zhang, "Subcycle overvoltage dynamics in solar pvs," *IEEE Trans. on Power Delivery*, vol. 36, pp. 1847–1858, 2021.

[8] A. Ekic, M. Maharjan, B. Strombeck, and D. Wu, "Impact of inverter modeling on sub-cycle dynamics in grid-connected solar pv systems," in *Proc. of the IEEE PVSC*, June 2021.

[9] A. Ghanavati, H. Lev-Ari, and A. M. Stanković, "A sub-cycle approach to dynamic phasors with application to dynamic power quality metrics," *IEEE Trans. on Power Delivery*, vol. 33, no. 5, pp. 2217–2225, 2018.

[10] K. W. Jones, P. Pourbeik *et al.*, "Impact of inverter based generation on bulk power system dynamics and short-circuit performance," *Task Force on Short-Circuit and System Performance Impact of Inverter Based Generation, Tech. Rep. PES-TR68*, Dec. 2018.

[11] H. Mohsenian-Rad, M. Kezunovic, and F. Rahmatian, "Synchro-waveforms in wide-area monitoring, control, and protection: Real-world examples and future opportunities," *IEEE Power and Energy Magazine*, vol. 23, no. 1, pp. 69–80, 2025.

[12] A. Ekic, B. Walberg, M. Maharjan *et al.*, "Impact of grid strength on sub-cycle dynamics in solar pv systems," in *IEEE PESGM*, Jul. 2021.

[13] C. Li, "Unstable operation of photovoltaic inverter from field experiences," *IEEE Trans. on Power Delivery*, vol. 33, pp. 1013–1015, 2017.

[14] W. Du, F. K. Tuffner, K. P. Schneider, R. H. Lasseter, J. Xie, Z. Chen, and B. Bhattarai, "Modeling of grid-forming and grid-following inverters for dynamic simulation of large-scale distribution systems," *IEEE Trans. on Power Delivery*, vol. 36, no. 4, pp. 2035–2045, 2021.

[15] P. P. Dash and M. kazerani, "Dynamic modeling and performance analysis of a grid-connected current-source inverter-based photovoltaic system," *IEEE Trans. on Sustainable Energy*, vol. 2, pp. 443–450, 2011.

[16] M. Ghazavi Dozein, B. C. Pal, and P. Mancarella, "Dynamics of inverter-based resources in weak distribution grids," *IEEE Trans. on Power Systems*, vol. 37, pp. 3682–3692, Jan 2022.

[17] H. Cai, J. Xiang, and W. Wei, "Modelling, analysis and control design of a two-stage photovoltaic generation system," *IET Renewable Power Generation*, vol. 10, no. 8, pp. 1195–1203, June 2016.

[18] W. Li, P. Chao, X. Liang, J. Ma, D.Xu, and X. Jin, "A practical equivalent method for DFIG wind farms," *IEEE Trans. on Sustainable Energy*, vol. 9, no. 2, pp. 610–620, Apr 2018.

[19] L. Fan, Z. Miao, S. Shah, P. Koralewicz, V.Gevorgian, and J. Fu, "Data-driven dynamic modeling in power systems: A fresh look on inverter-based resource modeling," *IEEE Power & Energy Magazine*, Jun 2022.

[20] P. Khaledian, A. Shahsavari, and H. Mohsenian-Rad, "Event-based dynamic response modeling of large behind-the-meter solar farms: A data-driven method based on real-world data," in *Proc. of the IEEE PES ISGT*, Washington, DC, Jan 2023.

[21] F. Ahmadi-Gorjayi and H. M. Rad, "Data-driven models for sub-cycle dynamic response of inverter-based resources using WMU measurements," *IEEE Trans. on Smart Grid*, vol. 14, pp. 4125–4128, Sep 2023.

[22] K. Mahapatra, S. Munikoti, and J. Folium, "Transmission data-driven user-defined model for inverter-based and conventional power plants," in *Proc. of the IEEE RWS*, Austin, TX, Dec. 2024.

[23] N. Mohammed, W. Zhou, B. Bahrani, and D. J. Hill, "Support vector machines for predicting the impedance model of inverter-based resources," *IEEE Trans. on Power Systems*, pp. 1–17, 2024.

[24] R. Khatua, A. Haldar, and et al., "A noninvasive measurement technique of grid and converter wideband impedance," *IEEE Trans. on Industrial Informatics*, vol. 20, no. 1, pp. 886–898, 2024.

[25] S. Biswas, F. Tuffner, J. Follum, and T. Wall, "Inverter model validation and calibration using phasor measurement unit data," *IEEE Access*, vol. 12, pp. 98990 - 99001, Jul. 2024.

[26] S. Hochreiter and J. Schmidhuber, "Long short-term memory," *Neural computation*, vol. 9, no. 8, pp. 1735–1780, 1997.

[27] Z. Shao, Q. Wang, Y. Cao, D. Cai, Y. You, and R. Lu, "A novel data-driven lstm-saf model for power systems transient stability assessment," *IEEE Trans. on Industrial Informatics*, vol. 20, pp. 9083–9097, 2024.

[28] Q. Wang, S. Bu, Z. He, and Z. Y. Dong, "Toward the prediction level of situation awareness for electric power systems using cnn-lstm network," *IEEE Trans. on Industrial Informatics*, vol. 17, pp. 6951–6961, 2021.

[29] X. Lin, R. Zamora, C. A. Baguley, and A. K. Srivastava, "A hybrid short-term load forecasting approach for individual residential customer," *IEEE Trans. on Power Delivery*, vol. 38, no. 1, pp. 26–37, 2023.

[30] A. Bhukya and C. Koley, "Bi-long short-term memory networks for radio frequency based arrival time detection of partial discharge signals," *IEEE Trans. on Power Delivery*, vol. 37, no. 3, pp. 2024–2031, 2022.

[31] M. Abdel-Nasser and K. Mahmoud, "Accurate photovoltaic power forecasting models using deep lstm-rnn," *Neural computing and applications*, vol. 31, pp. 2727–2740, 2019.

[32] V. Veerasamy, N. I. A. Wahab, M. L. Othman, and et al., "LSTM recurrent neural network classifier for high impedance fault detection in solar pv integrated power system," *IEEE Access*, vol. 9, pp. 32 672–32 687, 2021.

[33] P. Qashqai, R. Zgheib, and K. Al-Haddad, "GRU and LSTM comparison for black-box modeling of power electronic converters," in *Proc. of the Annual Conference of the IEEE Industrial Electronics Society*, 2021.

[34] H. Mohsenian-Rad, J.-Y. Joo, M. Balestrieri, L. Piyasinghe, S. Biswas, K. Chatterjee, H. Valizadeh-Haghi, K. Chang, J. Grappe, T. Laughner, S. Blair, C. Mullins, Y. Liu, Y. Wu, B. Sun, V. Choinière, H. Mohsenzadeh-Yazdi, F. Ahmadi-Gorjayi, L. Chen, J. Follum, Y. Seyedi, A. Karpilow, M. Paolone, M. J. Mousavi, S. R. Samantaray, J. Dagle, A. Wilson, C. Li, A. Shahsavari, M. Mohseni Bonab, A. Ragusa, M. R. Younis, B. Moussa, H. Ghoudjehbaklou, D. Deka, M. Farrokhabadi, F. Aminifar, C. Lackner, F. Rahmatian, R. Brown, and R. Kirby, "Synchro-waveform measurements and data analytics in power systems," Dec. 2024, https://live-ucr-ieeesynchrowaveformbcoe.pantheonsite.io/sites/default/files/2025-04/pes_tr_127_amps_1218724.pdf.

[35] N. Ehsani, F. Ahmadi-Gorjayi, Z.-J. Ye, A. McEachern, and H. Mohsenian-Rad, "Sub-cycle event detection and characterization in continuous streaming of synchro-waveforms: An experiment based on gridsweep measurements," in *in Proc. of the IEEE PES NAPS*, 2023.

[36] I. Khan, K. J. K. Hongbo Sun, J. Guo, and D. N. Nikovski, "Combined detection and localization model for high impedance fault under noisy condition," in *Proc. of the IEEE PESGM*, Orlando, FL, jul 2023.

[37] M. Izadi and H. Mohsenian-Rad, "Synchronous waveform measurements to locate transient events and incipient faults in power distribution networks," *IEEE Trans. on Smart Grid*, vol. 12, pp. 4295–4307, 2021.

[38] M. MansourLakouraj, H. Hosseinpour, H. Livani, and M. Benidris, "Waveform measurement unit-based fault location in distribution feeders via short-time matrix pencil method and graph neural network," *IEEE Trans. on Industry Applications*, vol. 59, no. 2, pp. 2661–2670, 2022.

[39] B. Gao, R. Torquato, W. Xu, and W. Freitas, "Waveform-based method for fast and accurate identification of subsynchronous resonance events," *IEEE Trans. on Power Systems*, vol. 34, no. 5, pp. 3626–3636, 2019.

[40] A. Ragusa, H. G. Sasse, and A. Duffy, "On-line partial discharge localization in power cables based on electromagnetic time reversal theory - numerical validation," *IEEE Trans. on Power Delivery*, vol. 37, pp. 2911–2920, 2022.

[41] H. Mohsenian-Rad, A. Shahsavari, and M. Majidi, "Analysis of power quality events for wildfire monitoring: Lessons learned from a california wildfire," in *Proc. of the IEEE PES ISGT*, San Juan, Puerto Rico, Nov. 2023.

[42] A. Karpilow, M. Paolone, A. Derviškadić, and G. Frigo, "Step change detection for improved rocof evaluation of power system waveforms," in *International Conference on SGSMA*, Split, Croatia, 2022.

[43] H. Mohsenzadeh-Yazdi, F. Ahmadi-Gorjayi, and H. Mohsenian-Rad, "Sub-Cycle Dynamics Modeling of IBRs Using LSTM Methods and Synchro-waveform Measurements," in *in Proc. of the IEEE PESGM*, Seattle, WA, Jul. 2024.

[44] F. Tao, H. Zhang, A. Liu, and A. Y. C. Nee, "Digital twin in industry: State-of-the-art," *IEEE Trans. on Industrial Informatics*, vol. 15, no. 4, pp. 2405–2415, 2019.

[45] H. Mohsenian-Rad, *Smart Grid Sensors: Principles and Applications*. Cambridge University Press, United Kingdom, Apr. 2022.

[46] Schweitzer Engineering Laboratories, *SynchroWave Event Software*. [Online]. Available: https://selinc.com/products/5601-2/

[47] T. M. Kodinariya, P. R. Makwana *et al.*, "Review on determining number of cluster in k-means clustering," *International Journal*, vol. 1, no. 6, pp. 90–95, 2013.

[48] J. M. Santos and M. Embrechts, "On the use of the adjusted rand index as a metric for evaluating supervised classification," in *Proc. of the International Conference on Artificial Neural Networks*. Limassol, Cyprus: Springer, 2009.
[49] X. Ying, "An overview of overfitting and its solutions," in *Journal of physics: Conference series*, vol. 1168, p. 022022, 2019.
[50] Manitoba Hydro International, *Simple Solar Farm Model*, June 2019. [Online]. Available: https://www.pscad.com/knowledge-base/article/521

Hossein Mohsenzadeh Yazdi (S'23) received the B.Sc. degree in electrical engineering from Isfahan University of Technology, Isfahan, Iran, in 2019, and the M.Sc. degree in electrical engineering from the University of Tehran, Tehran, Iran, in 2022. He is currently pursuing the Ph.D. degree in electrical engineering at the University of California, Riverside, CA, USA. His research interests include the application of data-driven techniques and machine learning in power systems, as well as the analysis of synchro-waveform measurements.

Fatemeh Ahmadi-Gorjayi (S'20) received the B.Sc. degree in electrical engineering from Sharif University of Technology, Tehran, Iran, in 2013, and the M.Sc. degree in MBA, Operation Management and Supply Chain from the department of Industrial Engineering at University of Tehran, Tehran, Iran in 2018. She has recently received her Ph.D. degree from the University of California, Riverside, CA, USA. Her research interests include state estimation, power system harmonics, power system planning, and data-driven applications in power system.

Hamed Mohsenian-Rad (M'09-SM'14-F'20) received the Ph.D. degree in electrical and computer engineering from the University of British Columbia, Vancouver, BC, Canada, in 2008. He is currently a Professor of electrical engineering and a Bourns Family Faculty Fellow at the University of California, Riverside, CA, USA. His research is on monitoring, data analysis, and optimization of power systems and smart grids. He is the author of the textbook *Smart Grid Sensors: Principles and Applications* by Cambridge University Press - 2022. He was the recipient of the National Science Foundation (NSF) CAREER Award, the Best Paper Award from the IEEE Power and Energy Society General Meeting, the Best Paper Award from the IEEE Conference on Smart Grid Communications, and a Technical Achievement Award from the IEEE Communications Society. He has been the PI or co-PI on seventeen million dollars research grants in the area of smart grid. He has served as Editor for the IEEE TRANSACTIONS ON POWER SYSTEMS, IEEE TRANSACTIONS ON SMART GRID and the IEEE POWER ENGINEERING LETTERS.